



# A simulation comparison of calibration functions for different sets of spectral filter passbands in the traditional pure rotational Raman lidar technique

Vladislav V. Gerasimov<sup>1,2</sup>

Received: 19 November 2019 / Accepted: 12 October 2020 / Published online: 23 October 2020  
© Springer-Verlag GmbH Germany, part of Springer Nature 2020

## Abstract

The accuracy of tropospheric temperature measurements with pure rotational Raman (PRR) lidars is affected by the collisional broadening of N<sub>2</sub> and O<sub>2</sub> PRR lines. In this paper, we intercompare nine calibration functions (CFs) in the traditional PRR lidar technique via simulation. Taking into account the PRR line broadening, the simulation is performed for five sets of spectral filters (SFs) with different passbands in a PRR lidar receiving system. For simplicity of calculations, the transmission function of each SF is approximated by a rectangular function on the wavenumber interval, within which a SF passes the bulk of the backscattered signal intensity in the corresponding PRR lidar channel. A narrow-linewidth laser operating at wavelengths of 354.67 and 532 nm is considered as a lidar transmitter. The CF best suited for tropospheric temperature retrievals from raw PRR lidar data for each set of SFs and laser wavelength is determined by comparative analysis of calibration errors  $\Delta T$  produced using these CFs. The absolute error  $|\Delta T|$  does not exceed the value of  $3 \times 10^{-3}$  K when using the best three-coefficient CF, while  $|\Delta T| < 4 \times 10^{-4}$  K for the best four-coefficient CF regardless of the laser wavelength and SF set used.

## 1 Introduction

In the pure rotational Raman (PRR) lidar technique, air temperature  $T$  is determined from a ratio  $Q(T)$  of backscattered signal intensities from two PRR spectrum bands of atmospheric molecules N<sub>2</sub> and O<sub>2</sub> [1–4]. For this reason, PRR lidars need to be calibrated and, therefore, a calibration function (CF) is required to retrieve temperature profiles from raw lidar signals. Several calibration methods aimed to improve temperature retrieval algorithms have been proposed in recent years [5, 6]. Behrendt et al. [7] made a correction for the elastic backscatter leakage into the nearest (to the laser line) PRR channel in the presence of cirrus clouds,

whereas Su et al. [8] did the same for both PRR channels. Chen et al. [9] presented a novel method that provides accurate PRR lidar calibration under the low signal-to-noise ratio conditions. The corrections for the incomplete laser beam receiver-field-of-view overlap in the atmospheric boundary layer were proposed in [10–12]. The use of nonlinear CFs was shown in [13, 14] to increase the accuracy of temperature retrievals, especially in the troposphere where N<sub>2</sub> and O<sub>2</sub> PRR lines are significantly broadened by molecular collisions [15–17].

Two new techniques allowing retrieving temperature without lidar calibration have also been recently proposed and deserve attention. Weng et al. [18] designed a single-line-extracted PRR lidar system that effectively detects two isolated N<sub>2</sub> PRR line signals together with the elastic backscatter signal. The system provides continuous temperature measurements without lidar calibration with external temperature measurement instruments (e.g., radiosondes). Mahagammulla Gamage et al. [19] reported on application of the Optimal Estimation Method (OEM) to retrieve temperature profiles along with instrumental (lidar) parameters from PRR lidar measurements. The PRR lidar technique that utilizes a reference temperature profile from an atmosphere model or radiosonde data for lidar calibration (determination of CF coefficients) is now called “traditional” one [19].

**Electronic supplementary material** The online version of this article (<https://doi.org/10.1007/s00340-020-07540-2>) contains supplementary material, which is available to authorized users.

✉ Vladislav V. Gerasimov  
gvvsnae@mail.ru

<sup>1</sup> V.E. Zuev Institute of Atmospheric Optics of Siberian Branch of the Russian Academy of Science, 1, Academician Zuev Square, 634055 Tomsk, Russia

<sup>2</sup> National Research Tomsk State University, 36, Lenina Ave, 634050 Tomsk, Russia

Both techniques [18, 19] have several advantages over the traditional PRR lidar one. For example, the OEM is computationally fast and practical for routine temperature retrievals. The same is valid for the single-line-extracted PRR lidar. However, the selection of the lidar system or retrieval method depends on the problem to solve. In some cases the traditional retrieval algorithm showed some advantages over the considered techniques. Analyzing the results presented in [18], one can see that the traditional algorithm more precisely retrieves temperatures from nighttime measurements and in the presence of cirrus clouds, whereas the OEM more precisely retrieves temperatures from daytime measurements and in the presence of low level clouds. Both  $1 - \sigma$  absolute statistical uncertainty of temperature retrieval and difference between retrieved and radiosonde profiles presented in [19] are much larger compared to those that can be provided by the traditional retrieval algorithm. Moreover, the accuracy of temperature retrievals with the traditional algorithm can always be increased by selecting a suitable CF [17].

The influence of passband widths of interference filters and their central wavelength positions in  $N_2$  and  $O_2$  PRR spectrum on the accuracy of temperature measurements using PRR lidars was analyzed in detail by Hammann and Behrendt [20]. However, the authors did not consider the PRR line broadening in their simulation. Conversely, the collisional broadening of  $N_2$  and  $O_2$  PRR lines was taken into account in [17], but only for one set of spectral filter (SF) passbands in a PRR lidar receiving system. In this study, we estimate the effect of collisional PRR line broadening on the accuracy of tropospheric (0–11 km) temperature measurements and intercompare nine nonlinear CFs in the traditional PRR lidar technique via simulation. The simulation is performed for five frequently used sets of SF passband widths and two laser wavelengths (354.67 and 532 nm). Note that the design features of PRR lidars are not taken into account in this study.

## 2 Calibration functions

### 2.1 General calibration function

According to the PRR lidar theory [1, 2, 4], a simple temperature dependence can be obtained only for the intensity ratio of any two individual PRR lines  $i$  and  $k$  from  $N_2$  and/or  $O_2$  PRR spectrum:

$$Q^{\text{indiv.}}(T) = \frac{I(J_i, T)}{I(J_k, T)} = \exp\left(\alpha + \frac{\beta}{T}\right). \quad (1)$$

Here,  $J_i$  and  $J_k$  are the rotational quantum numbers of the initial states of the PRR transitions corresponding to lines  $i$

and  $k$ , and  $\alpha$  and  $\beta$  are the constants defined from the theory. Taking the natural logarithm of Eq. (1), we have:

$$\ln Q^{\text{indiv.}}(T) = \alpha + \frac{\beta}{T} \Leftrightarrow y = \alpha + \beta x, \quad (2)$$

where  $x = 1/T$  is the reciprocal temperature and  $y = \ln Q^{\text{indiv.}}(T)$ . The desired temperature is easily derived from the ratio of intensities:

$$T = \frac{\beta}{\ln Q^{\text{indiv.}} - \alpha}. \quad (3)$$

In practical measurements, SFs in PRR channels of a lidar receiving system extract two bands from the backscattered light spectrum [4]. Both bands, containing several adjacent lines from the Stokes and/or anti-Stokes branches of  $N_2$  and  $O_2$  PRR spectrum, are selected so that the intensities of the lines entering them have the opposite temperature dependence (Fig. 1). The lines, corresponding to low ( $J_{\text{low}}$ ) and high ( $J_{\text{high}}$ ) rotational quantum numbers of the initial states of the PRR transitions, fall into the near and far (to the laser line) PRR channels (channels  $J_{\text{low}}$  and  $J_{\text{high}}$ ), respectively. The intensity of each  $N_2$  PRR line with  $J_{\text{low}} \leq 8$  ( $J_{\text{low}} \leq 11$  for  $O_2$  PRR lines) decreases with increasing temperature and, conversely, the intensity of  $N_2$  PRR lines with  $J_{\text{high}} \geq 9$  ( $J_{\text{high}} \geq 13$  for  $O_2$  PRR lines) increases with increasing temperature, in both branches of the spectrum. The choice of such lines makes it possible to minimize the overlap of the

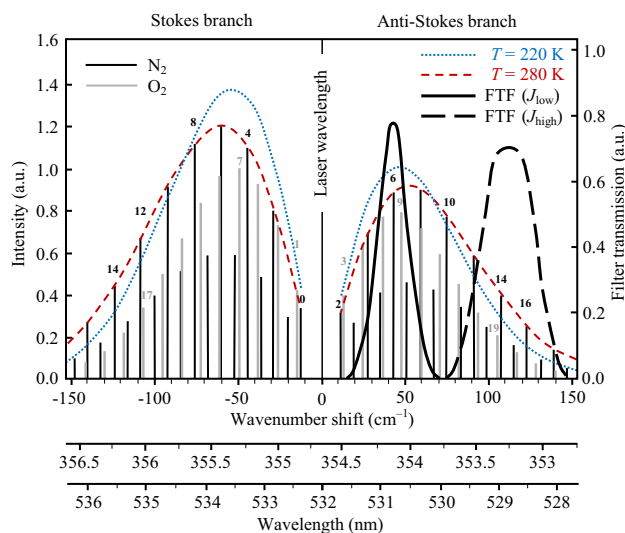


**Fig. 1** Equidistant PRR spectra of  $N_2$  and  $O_2$  linear molecules, schematic drawing of filter transmission functions (FTF), and envelopes of  $N_2$  PRR spectrum at different temperatures. The laser beam wavelengths are 354.67 and 532 nm. The index over a spectral line denotes the rotational quantum number  $J$  of the initial state of the transition. All PRR line intensities are normalized to the intensity of  $N_2$  PRR line with  $J=6$  of the anti-Stokes branch at  $T=220$  K

SF transmission functions of PRR channels (Fig. 1). Note that only odd lines beginning with odd  $J$  exist in  $O_2$  PRR spectrum [21]. Therefore, we have to consider the following ratio [2]:

$$Q^{\Sigma}(T) = \frac{I_{low}^{\Sigma}(T)}{I_{high}^{\Sigma}(T)} = \frac{\left[ \sum_{J_i} \sum_{i=N_2, O_2} I_i(J_i, T) \right]_{low}}{\left[ \sum_{J_i} \sum_{i=N_2, O_2} I_i(J_i, T) \right]_{high}}, \quad (4)$$

where  $I_i(J_i, T)$  are the intensities of  $N_2$  and  $O_2$  individual PRR lines, corresponding to rotational quantum numbers  $J_i$ ,  $I_{low}^{\Sigma}(T)$  and  $I_{high}^{\Sigma}(T)$  are the overall intensities of the PRR lines that enter the corresponding channels  $J_{low}$  and  $J_{high}$ , indices “low” and “high” show that summations in the numerator and denominator refer to the corresponding PRR spectrum bands.

The right side of Eq. (4) represents the ratio of the sums of exponential expressions that cannot be reduced to a simple function of temperature and, therefore, the intensity ratio  $Q^{\Sigma}(T)$  needs to be calibrated. Arshinov et al. [2] proposed the simplest (linear) CF in the form of Eq. (2) and, hence, the air temperature is determined from the ratio  $Q^{\Sigma}(T)$  similarly to Eq. (3):

$$T = \frac{B_0}{\ln Q^{\Sigma} - A_0}, \quad (5)$$

where  $A_0$  и  $B_0$  are the calibration (fit) coefficients. To reduce the statistical uncertainties of temperature retrievals, the second-order polynomial was proposed in [13] to be used as a CF:

$$\ln Q^{\Sigma} = A_1 + \frac{B_1}{T} + \frac{C_1}{T^2} \quad \Leftrightarrow \quad y = A_1 + B_1x + C_1x^2, \quad (6)$$

where  $A_1$ ,  $B_1$  and  $C_1$  are the calibration coefficients. The other types of CFs have been used for temperature retrievals in [3, 4, 14–17].

Equations (1)–(6) were obtained under the assumption that PRR lines are not broadened and, therefore, their profiles are described by the Dirac function. In fact, PRR lines are broadened due to both Doppler and molecular collision effects. PRR lines broadened only by the Doppler effect have a Gaussian profile, whereas the lines broadened only due to molecular collisions have a Lorentzian profile. The real PRR line profiles are described by a Voigt function that takes into account both types of broadening [22]. The molecular collision effect dominates over the Doppler one in the troposphere (Fig. 2) and the Lorentzian profile wings are higher than those of the Gaussian of the same full width at half maximum (FWHM) [22].

Owing to the long Lorentzian tails, each broadened PRR line  $j$  lying outside the SF passbands leads to the parasitic signal leakage into both PRR channels (Fig. 3). At the same

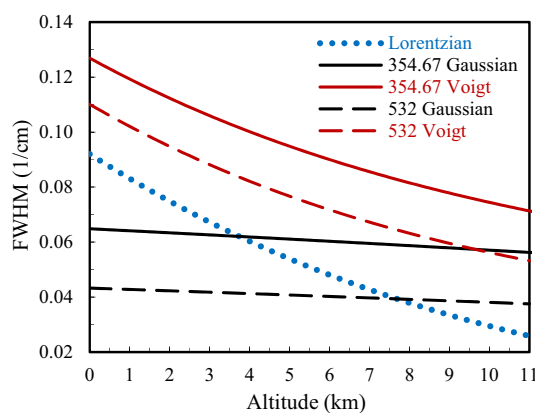


Fig. 2 FWHMs of the Gaussian, Lorentzian, and Voigt profiles of  $N_2$  PRR line (with  $J=6$  of the anti-Stokes branch) for the laser wavelengths of 354.67 and 532 nm. The dependence of temperature on altitude is set by the tropospheric (0–11 km) temperature profile of the U.S. Standard Atmosphere (1976)

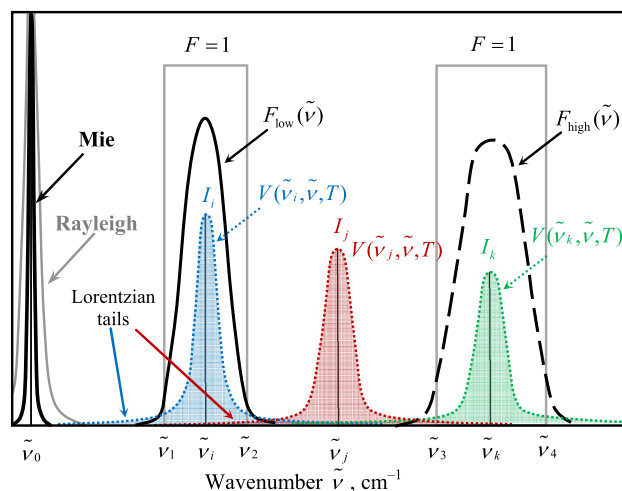


Fig. 3 A schematic drawing (not to scale) of Voigt profiles of broadened PRR lines  $i, j, k$  and filter transmission functions (see Sect. 3.1)  $F_{low}(\tilde{\nu})$  and  $F_{high}(\tilde{\nu})$  of lidar channels  $J_{low}$  and  $J_{high}$  approximated by a rectangle function  $F=1$ . The wavenumber  $\tilde{\nu}_0$  and intervals  $(\tilde{\nu}_1; \tilde{\nu}_2)$  and  $(\tilde{\nu}_3; \tilde{\nu}_4)$  correspond to the laser line and passbands of channels  $J_{low}$  and  $J_{high}$ , respectively

time, the collisional broadening of any PRR lines  $i$  and  $k$  lying inside lidar channels  $J_{low}$  and  $J_{high}$ , respectively, results in both parasitic signal leakage into neighboring PRR channel and desired signal loss in both channels. The PRR lidar CF that takes into account the collisional broadening of all PRR lines was derived in the general analytical form in [15]:

$$\ln Q(T) = \sum_{n=-\infty}^{\infty} \alpha_n T^{\frac{n}{2}}, \quad (7)$$

where  $\alpha_n$  are the calibration coefficients.

### 2.2 Temperature retrieval functions

To obtain temperature profiles from raw lidar signals, a temperature retrieval function (TRF)  $T=T(Q)$  derived from the selected CF  $Q=Q(T)$  is required in the traditional retrieval algorithm. In the case of the linear (2) and quadratic (6) CFs, the corresponding TRFs are easily derived. When choosing the third-order polynomial in  $1/T$  as a CF, it is necessary to solve a cubic equation, the presence and number of real roots of which depend on the signs of the polynomial coefficients. Hence, any CF requiring solving a  $n$ -order equation ( $n \geq 3$ ) to derive the corresponding TRF can hardly be used for temperature retrieval. As seen from Eq. (7), the general CF is a series and cannot be directly used in the temperature retrieval algorithm. For this reason, nine nonlinear CFs representing simple special cases of Eq. (7) were considered in [17]. All the special cases take the collisional broadening of  $N_2$  and  $O_2$  PRR lines into account in varying degrees. Below we give only the TRFs required for this study without specifying their initial nonlinear CFs. Since the linear CF completely ignores PRR line broadenings and its corresponding TRF retrieves temperature with larger errors (uncertainties) compared to other TRFs derived from nonlinear CFs [4, 15–17], we will not consider Eqs. (2) and (5). Each TRF  $i$  and its calibration constants  $A_i, B_i, C_i, etc.$  are numbered ( $i=1, 2, \dots, 9$ ) as in [17].

Let us consider three-coefficient TRFs, the first of which (TRF 1) is derived from the CF (6) proposed in [13]:

$$T = \frac{2C_1}{-B_1 + \sqrt{B_1^2 + 4C_1(\ln Q - A_1)}}. \tag{8}$$

TRF 2 corresponds to a CF proposed in [15]:

$$T = \frac{2B_2}{(\ln Q - A_2) + \sqrt{(\ln Q - A_2)^2 - 4B_2C_2}}. \tag{9}$$

TRF 3 was first applied in [14]:

$$T = \frac{C_3}{(\ln Q)^2 + B_3 \ln Q + A_3}. \tag{10}$$

TRF 4 is derived from a CF proposed in [15]:

$$T = \frac{\ln Q}{B_4(\ln Q)^2 + A_4 \ln Q + C_4}. \tag{11}$$

The following two functions (TRFs 5 and 6) with three calibration constants were first used in [17]:

$$T = \left[ \frac{2C_5}{-B_5 + \sqrt{B_5^2 + 4C_5(\ln Q - A_5)}} \right]^2, \tag{12}$$

$$T = \left[ \frac{2B_6}{(\ln Q - A_6) + \sqrt{(\ln Q - A_6)^2 - 4B_6C_6}} \right]^2. \tag{13}$$

TRFs 7, 8, and 9 with four calibration constants were also first proposed and used in [17]:

$$T = \frac{D_7}{(\ln Q)^3 + C_7(\ln Q)^2 + B_7 \ln Q + A_7}, \tag{14}$$

$$T = \frac{(\ln Q)^2}{B_8(\ln Q)^3 + A_8(\ln Q)^2 + C_8 \ln Q + D_8}, \tag{15}$$

$$T = \frac{\ln Q}{C_9(\ln Q)^3 + B_9(\ln Q)^2 + A_9 \ln Q + D_9}. \tag{16}$$

The CFs which are initial for TRFs 1–9 along with the equations for the absolute and relative statistical uncertainties of temperature retrievals can be found in [17] and in the electronic supplementary material (Table S1).

### 3 Numerical simulation technique

In the next three Sects. 3.1–3.3, we make some assumptions to simplify the numerical calculation of the intensity ratio  $Q=Q(T)$ .

#### 3.1 Spectral filter transmission functions

Let us consider only the anti-Stokes branch of  $N_2$  and  $O_2$  PRR spectrum for definiteness. Due to the broadening of PRR lines and their contribution to the signals detected in both lidar channels, we can write [15] for the intensity ratio instead of Eq. (4):

$$Q^{\text{all}}(T) = \frac{I_{\text{low}}^{\text{all}}(T)}{I_{\text{high}}^{\text{all}}(T)} = \frac{\sum_{J_i} \sum_{i=N_2, O_2} [I_i(J_i, T) \cdot X_{\text{low}}^i(\tilde{\nu}_i, T)]}{\sum_{J_i} \sum_{i=N_2, O_2} [I_i(J_i, T) \cdot X_{\text{high}}^i(\tilde{\nu}_i, T)]}. \tag{17}$$

Here, the summations are carried out over all rotational quantum numbers  $J_i$  of the initial states of  $N_2$  and  $O_2$  PRR transitions,  $\tilde{\nu}_i = \tilde{\nu}(J_i)$  and  $I_i(J_i, T)$  are the central wavenumber and total intensity of  $i$  broadened PRR line with  $J_i$ , respectively. The functions  $X_{\text{low}}^i$  and  $X_{\text{high}}^i$  describe the fractions of the intensity  $I_i(J_i, T)$  that fall within the SF passbands of channels  $J_{\text{low}}$  and  $J_{\text{high}}$ , respectively, and  $I_{\text{low}}^{\text{all}}(T)$  and  $I_{\text{high}}^{\text{all}}(T)$  are the overall intensities detected in the corresponding lidar channels (with contributions from all broadened

lines). The functions  $X_{low}^i$  and  $X_{high}^i$  are defined by the following expressions:

$$X_{low}^i(\tilde{\nu}_i, T) = \int_0^{+\infty} F_{low}(\tilde{\nu}) \cdot V(\tilde{\nu}_i, \tilde{\nu}, T) d\tilde{\nu}, \tag{18}$$

$$X_{high}^i(\tilde{\nu}_i, T) = \int_0^{+\infty} F_{high}(\tilde{\nu}) \cdot V(\tilde{\nu}_i, \tilde{\nu}, T) d\tilde{\nu}, \tag{19}$$

where  $F_{low}(\tilde{\nu})$  and  $F_{high}(\tilde{\nu})$  are the SF transmission functions of channels  $J_{low}$  and  $J_{high}$ , respectively, and  $V(\tilde{\nu}_i, \tilde{\nu}, T)$  is the Voigt profile of  $i$  broadened PRR line (Fig. 3).

There are several ways to approximate SF transmission functions by an analytical expression. For example,  $F_{low}(\tilde{\nu})$  and  $F_{high}(\tilde{\nu})$  are approximated by a Gaussian function [3] or by the function proposed in [23]. However, this complicates the calculation of integrals (18) and (19) and, therefore, ratio (17). As shown in [15], the SF transmission functions can be approximated by a piecewise-constant (staircase) function with any desired accuracy. To further simplify the calculations, the staircase function can be replaced by a constant one on the wavenumber interval, within which a SF passes the bulk of the backscattered signal intensity in the corresponding PRR channel (Fig. 3). For example, in the case of channel  $J_{low}$  we can write:

$$F_{low}(\tilde{\nu}) = \begin{cases} 0, & \tilde{\nu} \leq \tilde{\nu}_1 \\ F = \text{const}, & \tilde{\nu} \in (\tilde{\nu}_1; \tilde{\nu}_2), \\ 0, & \tilde{\nu} \geq \tilde{\nu}_2 \end{cases} \tag{20}$$

where  $(\tilde{\nu}_1; \tilde{\nu}_2)$  is the SF passband of the lidar channel. Without loss of generality, we can also put  $F = 1$  for both SF transmission functions, and then instead of Eqs. (18) and (19) we get:

$$X_{low}^i(\tilde{\nu}_i, T) = \int_{\tilde{\nu}_1}^{\tilde{\nu}_2} V(\tilde{\nu}_i, \tilde{\nu}, T) d\tilde{\nu}, \tag{21}$$

$$X_{high}^i(\tilde{\nu}_i, T) = \int_{\tilde{\nu}_3}^{\tilde{\nu}_4} V(\tilde{\nu}_i, \tilde{\nu}, T) d\tilde{\nu}, \tag{22}$$

where  $(\tilde{\nu}_3; \tilde{\nu}_4)$  is the SF passband of channel  $J_{high}$ . Note that one can choose to use the FWHMs of the SF transmission functions as the SF passbands  $(\tilde{\nu}_1; \tilde{\nu}_2)$  and  $(\tilde{\nu}_3; \tilde{\nu}_4)$ .

### 3.2 PRR line profiles

The backscatter profile of  $i$  PRR line inhomogeneously broadened only due to the Doppler effect is known to be described by a Gaussian function (normal distribution) [22]:

$$G(\tilde{\nu}_i, \tilde{\nu}, T) = \frac{1}{\gamma_G^i \sqrt{2\pi}} \exp \left[ -\frac{(\tilde{\nu} - \mu_i)^2}{2(\gamma_G^i)^2} \right]. \tag{23}$$

Here,  $\mu_i = \tilde{\nu}_i$  (cm<sup>-1</sup>) is the mathematical expectation (the central wavenumber of the line profile), and  $\gamma_G^i$  (cm<sup>-1</sup>) is the standard deviation defined by the equation:

$$\gamma_G^i = \tilde{\nu}_i \sqrt{\frac{k_B T}{m_{air} c^2}}, \tag{24}$$

where  $k_B$  is the Boltzmann constant,  $m_{air}$  is the average mass of air molecules, and  $c$  is the speed of light. The FWHM of the Gaussian profile is defined as:

$$\Delta\tilde{\nu}_{i,G}^{FWHM} = 2\sqrt{2 \ln 2} \cdot \gamma_G^i. \tag{25}$$

The backscatter profile of  $i$  PRR line homogeneously broadened only by molecular collisions is described by a Lorentzian function (Cauchy distribution) that is defined for the angular frequency  $\omega$  (rad/s) [22]:

$$L(\omega_i, \omega, T) = \frac{1}{\pi} \cdot \frac{\gamma_L}{(\omega - \omega_i)^2 + \gamma_L^2}, \tag{26}$$

where  $\omega_i$  is the central angular frequency of the line profile, and  $\gamma_L$  (rad/s) specifies the half width at half maximum (HWHM) of the Lorentzian profile. Subsequently, the FWHM (rad/s) of the Lorentzian profile is defined as:

$$\Delta\omega_L^{FWHM} = 2\gamma_L. \tag{27}$$

After the substitution  $\omega = 2\pi c\tilde{\nu}$ , the Lorentzian function (26) can be expressed as a function of wavenumber:

$$L(\tilde{\nu}_i, \tilde{\nu}, T) = \frac{1}{\pi} \cdot \frac{\gamma_L / (2\pi c)}{(\tilde{\nu} - \tilde{\nu}_i)^2 + (\gamma_L / (2\pi c))^2} \tag{28}$$

with the corresponding FWHM defined in cm<sup>-1</sup>:

$$\Delta\tilde{\nu}_L^{FWHM} = \frac{\Delta\omega_L^{FWHM}}{2\pi c} = \frac{\gamma_L}{\pi c}, \tag{29}$$

where  $c$  is the speed of light in cm/s. For a two-component gas (e.g., a mixture of N<sub>2</sub> and O<sub>2</sub> molecules in air), the



formula for estimation of the FWHM (29) in  $\text{cm}^{-1}$  at each altitude  $z$  can be written as follows:

$$\Delta\tilde{\nu}_L^{\text{FWHM}} = p_1^2 n_{\text{air}} d_1^2 \sqrt{\frac{8k_B T}{\pi \mu_1 c^2}} + 2p_1 p_2 n_{\text{air}} d_{12}^2 \sqrt{\frac{8k_B T}{\pi \mu_{12} c^2}} + p_2^2 n_{\text{air}} d_2^2 \sqrt{\frac{8k_B T}{\pi \mu_2 c^2}}, \tag{30}$$

where  $p_1 = 0.7809$  and  $p_2 = 0.2095$  are the probabilities to find  $\text{N}_2$  and  $\text{O}_2$  molecules in the homosphere (0–100 km), respectively;  $n_{\text{air}}$  is the air molecular number density;  $d_1$ ,  $d_2$ , and  $d_{12} = (d_1 + d_2)/2$  are the effective optical collision diameters in  $\text{N}_2$ – $\text{N}_2$ ,  $\text{O}_2$ – $\text{O}_2$ , and  $\text{N}_2$ – $\text{O}_2$  collisions, respectively;  $\mu_1 = m_1/2$ ,  $\mu_2 = m_2/2$ , and  $\mu_{12} = m_1 m_2 / (m_1 + m_2)$  are the

$3.05 \times 10^{-6} \text{ cm}^{-1}$  for the pure Lorentzian function (when  $\Delta\tilde{\nu}_{i,G}^{\text{FWHM}} = 0$ ).

$$X_{\text{low}}^i(\tilde{\nu}_i, T) = \frac{1}{\pi} \int_{\tilde{\nu}_1}^{\tilde{\nu}_2} \frac{\gamma_L / (2\pi c)}{(\tilde{\nu} - \tilde{\nu}_i)^2 + (\gamma_L / (2\pi c))^2} d\tilde{\nu} = \frac{1}{\pi} \left[ \arctan \left( \frac{\tilde{\nu}_2 - \tilde{\nu}_i}{\gamma_L / (2\pi c)} \right) - \arctan \left( \frac{\tilde{\nu}_1 - \tilde{\nu}_i}{\gamma_L / (2\pi c)} \right) \right], \tag{33}$$

reduced masses of colliding molecules in  $\text{N}_2$ – $\text{N}_2$ ,  $\text{O}_2$ – $\text{O}_2$ , and  $\text{N}_2$ – $\text{O}_2$  collisions, respectively. The temperature dependence of the effective optical collision diameters is described by Sutherland’s formula. Considering only binary collisions of molecules, for  $i$  atmospheric gas we have [24]:

$$d_i^2(T) = d_{i,\infty}^2 (1 + \Phi_i / T), \tag{31}$$

where  $d_{i,\infty}$  is the effective optical collision diameter at  $T \rightarrow \infty$ , and  $\Phi_i$  is the constant having the dimension of temperature (K).

The backscatter profile of  $i$  PRR line broadened by both Doppler effect and molecular collisions is described by a Voigt function. The function represents the convolution of Gaussian and Lorentzian functions and can only be calculated numerically [22]. For this reason, pseudo-Voigt functions, the linear combinations of the Gaussian and Lorentzian functions, are often used to approximate the Voigt ones. To estimate the FWHM (in  $\text{cm}^{-1}$ ) of a pseudo-Voigt function, one can apply the approximation formula proposed in [25]:

$$\Delta\tilde{\nu}_{i,V}^{\text{FWHM}} \approx 0.5346 \Delta\tilde{\nu}_L^{\text{FWHM}} + \sqrt{(\Delta\tilde{\nu}_{i,G}^{\text{FWHM}})^2 + 0.2166 (\Delta\tilde{\nu}_L^{\text{FWHM}})^2}. \tag{32}$$

This approximation has zero error for the pure Gaussian function (when  $\Delta\tilde{\nu}_L^{\text{FWHM}} = 0$ ) and an error of about

Since the Voigt profile shape in its wings is very close to the Lorentzian one and the boundaries of SF passbands are mostly located in the wings of PRR lines (Fig. 3), it is reasonable to use  $L(\tilde{\nu}_i, \tilde{\nu}, T)$  (28) instead of  $V(\tilde{\nu}_i, \tilde{\nu}, T)$  for a PRR line shape description [15]. Hence, instead of integrals (21) and (22) we can write:

$$X_{\text{high}}^i(\tilde{\nu}_i, T) = \frac{1}{\pi} \left[ \arctan \left( \frac{\tilde{\nu}_4 - \tilde{\nu}_i}{\gamma_L / (2\pi c)} \right) - \arctan \left( \frac{\tilde{\nu}_3 - \tilde{\nu}_i}{\gamma_L / (2\pi c)} \right) \right], \tag{34}$$

which can be easily calculated. Nevertheless, when calculating  $X_{\text{low}}^i$  and  $X_{\text{high}}^i$ , we use the HWHM  $\Delta\tilde{\nu}_{i,V}^{\text{FWHM}} / 2$  of the pseudo-Voigt function instead of the Lorentzian HWHM  $\gamma_L / (2\pi c)$ . This allows more accurate taking into account the contribution of broadened PRR lines to both lidar channels.

### 3.3 PRR line intensity

The intensity  $I_i(J_i, T)$  of an individual PRR line can be expressed as [26]:

$$I_i(J_i, T) = PL\beta_{\pi,i}(J_i, T) = PLn_i\sigma_{\pi,i}(J_i, T) = PLn_{\text{air}}p_i\sigma_{\pi,i}(J_i, T), \tag{35}$$

where  $P$  is the average power of the incident laser beam,  $L$  is the length of the scattering volume,  $\beta_{\pi,i}(J_i, T)$  is the backscatter cross-section (atmospheric backscatter coefficient),  $\sigma_{\pi,i}(J_i, T)$  is the differential backscatter cross-section, and  $n_i = p_i n_{\text{air}}$  is the partial number density of air component  $i$ . Substituting Eqs. (33), (34), and (35) into Eq. (17), we obtain for the intensity ratio:

$$Q(T) = \frac{\sum_{J_i} \sum_{i=\text{N}_2, \text{O}_2} \left\{ p_i \sigma_{\pi,i}(J_i, T) \left[ \arctan \left( \frac{\tilde{\nu}_2 - \tilde{\nu}_i}{\Delta\tilde{\nu}_{i,V}^{\text{FWHM}} / 2} \right) - \arctan \left( \frac{\tilde{\nu}_1 - \tilde{\nu}_i}{\Delta\tilde{\nu}_{i,V}^{\text{FWHM}} / 2} \right) \right] \right\}}{\sum_{J_i} \sum_{i=\text{N}_2, \text{O}_2} \left\{ p_i \sigma_{\pi,i}(J_i, T) \left[ \arctan \left( \frac{\tilde{\nu}_4 - \tilde{\nu}_i}{\Delta\tilde{\nu}_{i,V}^{\text{FWHM}} / 2} \right) - \arctan \left( \frac{\tilde{\nu}_3 - \tilde{\nu}_i}{\Delta\tilde{\nu}_{i,V}^{\text{FWHM}} / 2} \right) \right] \right\}}. \tag{36}$$

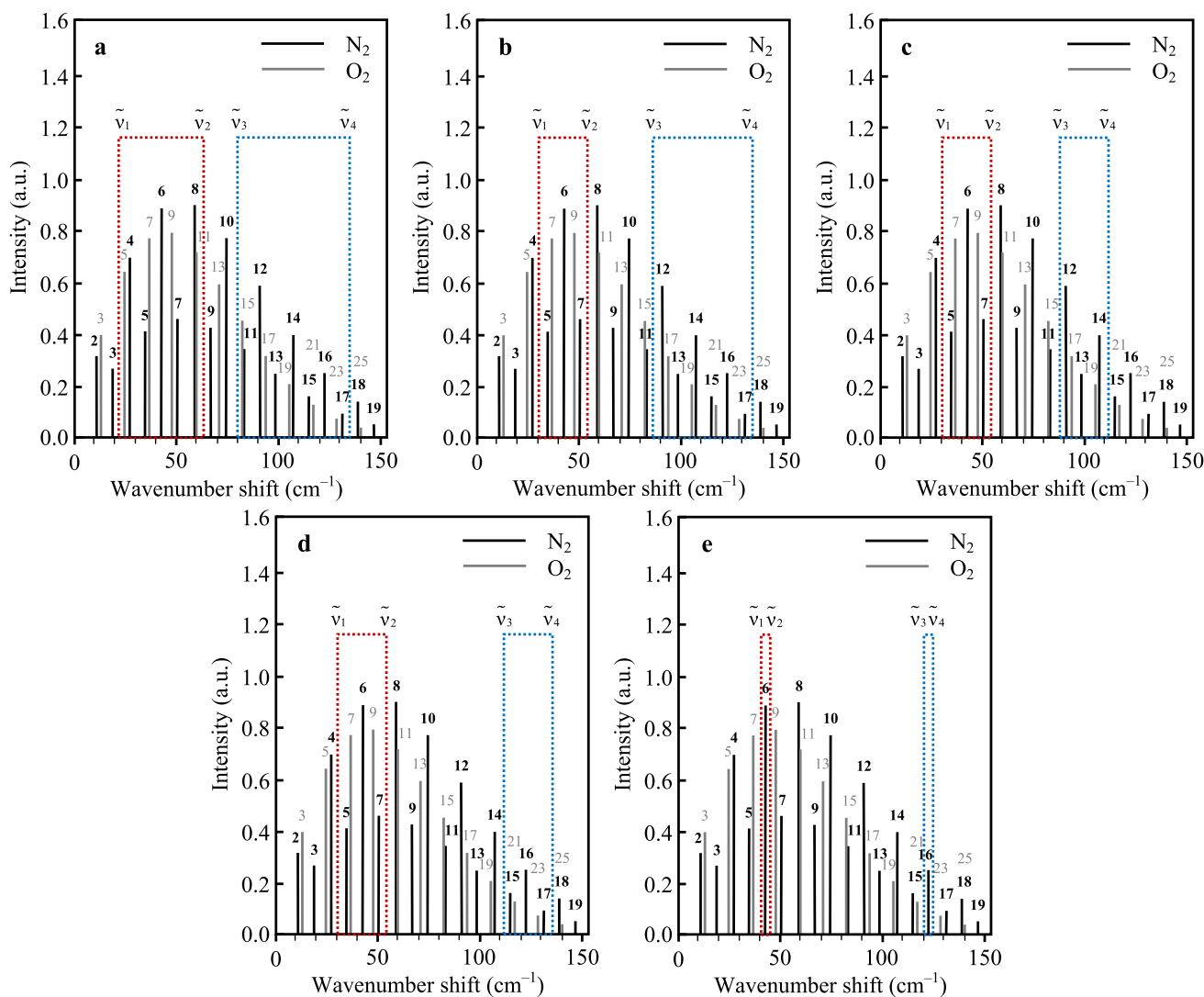


**Fig. 4** a–e Sets 1–5 of SF passbands ( $\tilde{\nu}_1; \tilde{\nu}_2$ ) and ( $\tilde{\nu}_3; \tilde{\nu}_4$ ) with equal transmission function  $F=1$  in lidar channels  $J_{low}$  and  $J_{high}$ , respectively. The index over a spectral line denotes the rotational quantum

number  $J$  of the initial state of the transition.  $N_2$  and  $O_2$  PRR spectrum corresponds to  $T=280$  K

### 4 Initial conditions for the simulation

Let us consider five sets of SF passbands that are mostly used in PRR lidar receiving systems (Fig. 4). We assume that a SF has a narrow passband if its width  $\Delta\tilde{\nu} \leq 25$   $cm^{-1}$  and a wide one at  $\Delta\tilde{\nu} > 40$   $cm^{-1}$ . The first set consists of SFs with wide passbands in both channels  $J_{low}$  and  $J_{high}$  [27–30]. The second set has a SF with a narrow passband in channel  $J_{low}$  and a SF with a wide passband in channel  $J_{high}$  [13, 23, 31, 32]. The third and fourth sets consist of SFs with equal narrow passbands in both PRR channels [5, 8, 16, 33], but with different central wavenumber positions in channel  $J_{high}$ . The

fifth set has two SFs with very narrow passbands provided by a Fabry–Perot interferometer [18]. The SF passbands ( $\tilde{\nu}_1; \tilde{\nu}_2$ ) and ( $\tilde{\nu}_3; \tilde{\nu}_4$ ) of channels  $J_{low}$  and  $J_{high}$ , their widths  $\Delta\tilde{\nu}$ , and  $N_2$  and  $O_2$  PRR lines (with  $J$ ) falling into the channels are shown in Table 1.

A narrow-linewidth ( $\sim 0.001$   $cm^{-1}$ ) laser operating at wavelengths of 354.67 and 532 nm is considered as a PRR lidar transmitter in the simulation. Such a linewidth can be ignored compared to the widths of PRR lines broadened by both Doppler effect and molecular collisions (Fig. 2). We take into account the contribution from 56  $N_2$  and  $O_2$  PRR lines to the signals detected in channels

**Table 1** Parameters of spectral filter passbands (SFPs)

	SFP set 1		SFP set 2		SFP set 3		SFP set 4		SFP set 5	
	$(\tilde{\nu}_1; \tilde{\nu}_2)$	$(\tilde{\nu}_3; \tilde{\nu}_4)$	$(\tilde{\nu}_1; \tilde{\nu}_2)$	$(\tilde{\nu}_3; \tilde{\nu}_4)$	$(\tilde{\nu}_1; \tilde{\nu}_2)$	$(\tilde{\nu}_3; \tilde{\nu}_4)$	$(\tilde{\nu}_1; \tilde{\nu}_2)$	$(\tilde{\nu}_3; \tilde{\nu}_4)$	$(\tilde{\nu}_1; \tilde{\nu}_2)$	$(\tilde{\nu}_3; \tilde{\nu}_4)$
SFP ( $\text{cm}^{-1}$ )	(23;65)	(80;135)	(30;55)	(85;135)	(30;55)	(87;112)	(30;55)	(112;137)	(43.2;44.3)	(122.8;123.9)
SFP width $\Delta\tilde{\nu}$ ( $\text{cm}^{-1}$ )	42	55	25	50	25	25	25	25	1.1	1.1
N <sub>2</sub> lines	5 lines $J=4, 5, 6, 7, 8$	7 lines $J=11, 12, 13, \dots, 17$	3 lines $J=5, 6, 7$	6 lines $J=12, 13, 14, \dots, 17$	3 lines $J=5, 6, 7$	3 lines $J=12, 13, 14$	3 lines $J=5, 6, 7$	3 lines $J=15, 16, 17$	3 lines $J=5, 6, 7$	1 line $J=16$
O <sub>2</sub> lines	4 lines $J=5, 7, 9, 11$	5 lines $J=15, 17, 19, 21, 23$	2 lines $J=7, 9$	4 lines $J=17, 19, 21, 23$	2 lines $J=7, 9$	2 lines $J=17, 19$	2 lines $J=7, 9$	2 lines $J=21, 23$	2 lines $J=7, 9$	1 line $J=16$

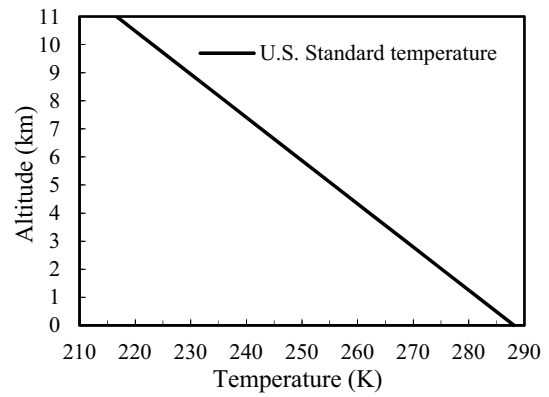


**Fig. 5** Tropospheric temperature profile of the U.S. Standard Atmosphere (1976)

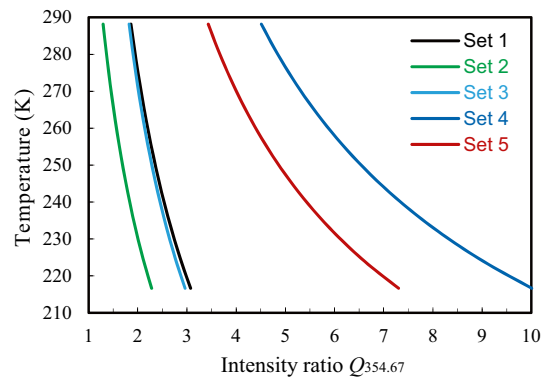


**Fig. 6** Tropospheric temperature vs intensity ratios  $Q_{354.67}$  calculated for five sets of SF passbands (Fig. 4)

$J_{\text{low}}$  and  $J_{\text{high}}$ . These lines include the first 34 N<sub>2</sub> lines with  $J=0, 1, \dots, 16$  (Stokes branch) and  $J=2, 3, \dots, 18$  (anti-Stokes branch) and 22 O<sub>2</sub> lines with  $J=1, 3, \dots, 21$  and  $J=3, 5, \dots, 23$  in the Stokes and anti-Stokes branches, respectively. The values of the constants required for calculating the FWHMs and/or HWHMs of the Gaussian (25), Lorentzian (30), and pseudo-Voigt (32) profiles are the following:  $m_{\text{air}} = 4.81 \times 10^{-26}$  kg,  $m_1 = 4.65 \times 10^{-26}$  kg,  $m_2 = 5.31 \times 10^{-26}$  kg,  $d_{1,\infty} = 3.51 \times 10^{-10}$  m,  $d_{2,\infty} = 3.52 \times 10^{-10}$  m,  $d_{12,\infty} \approx 3.515 \times 10^{-10}$  m [34],  $\Phi_1 = 105$  K (for N<sub>2</sub>-N<sub>2</sub> collisions),  $\Phi_2 = 125$  K (for O<sub>2</sub>-O<sub>2</sub> collisions), and  $\Phi_{12} = 115$  K (for N<sub>2</sub>-O<sub>2</sub> collisions) [24]. The tropospheric (0–11 km) temperature profile of the U.S. Standard Atmosphere (1976) [35] is used as a reference profile (Fig. 5) to set the dependence of temperature on altitude in Eqs. (24), (30)–(36) and to determine the calibration coefficients of TRFs 1–9 using the least squares method. The formulas and all the necessary constants for calculating the cross-sections  $\sigma_{\pi,i}(J_i, T)$  and intensity ratio (36) can be found in [4].



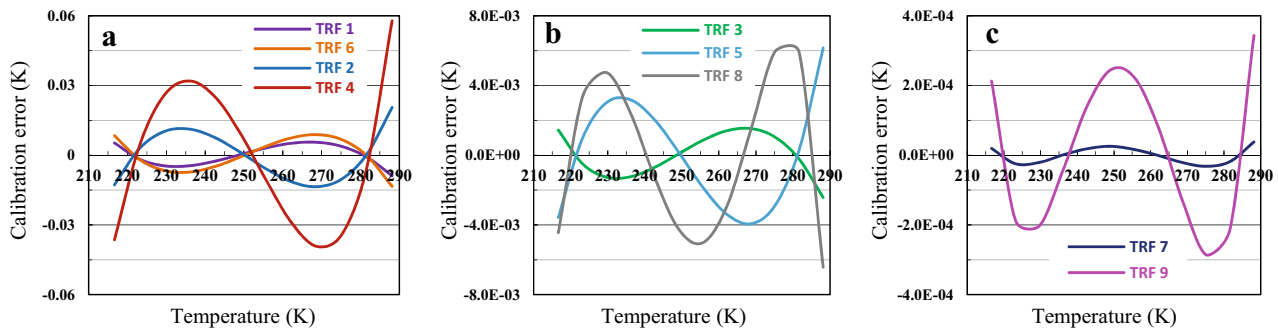


Fig. 7 Calibration errors  $\Delta T_{354.67}$  produced using TRFs 1–9 for SFP set 1 at  $\lambda = 354.67$  nm

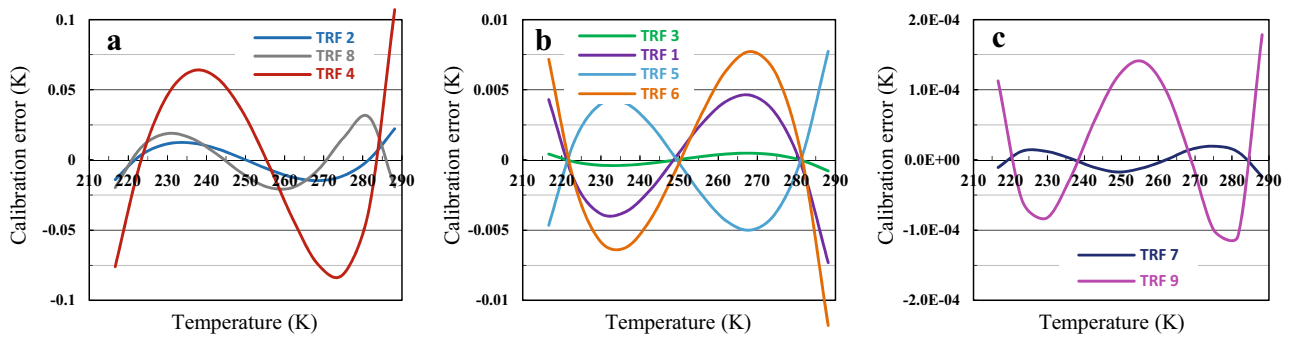


Fig. 8 Calibration errors  $\Delta T_{354.67}$  produced using TRFs 1–9 for SFP set 2 at  $\lambda = 354.67$  nm

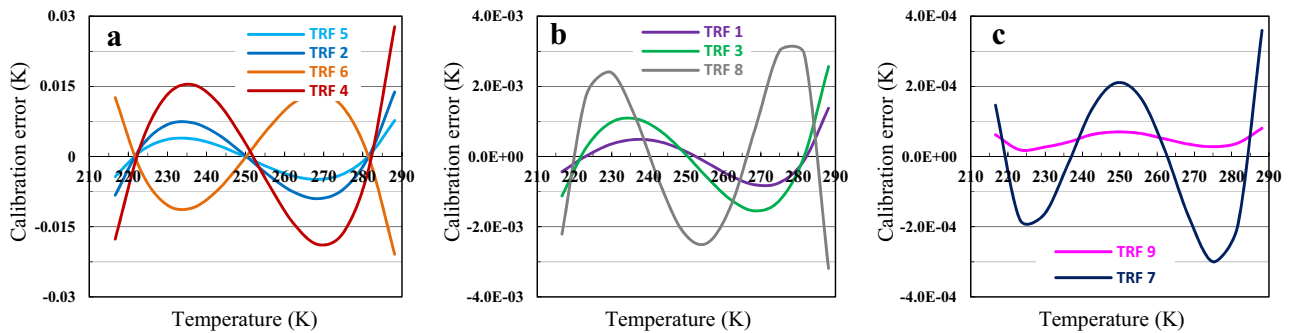


Fig. 9 Calibration errors  $\Delta T_{354.67}$  produced using TRFs 1–9 for SFP set 3 at  $\lambda = 354.67$  nm

### 5 Simulation results for $\lambda = 354.67$ nm

The simulation results for a laser wavelength of 354.67 nm are shown in Figs. 6, 7, 8, 9, 10 and 11. Figure 6 presents the dependences of tropospheric temperature on the intensity ratios  $Q_{354.67}$  calculated for five sets of SF passbands (Fig. 4, Table 1) using Eq. (36) under the conditions described above. To determine the best TRF for each of SFP sets 1–5, we intercompare temperature errors produced using TRFs 1–9. A temperature error (or calibration error)  $\Delta T$  is defined

as the difference between an ideal model profile and a temperature profile  $T = T(Q)$  retrieved from a simulated intensity ratio  $Q$  by one of the TRFs. The function that retrieves temperature with the smallest maximum calibration error in the troposphere will be considered as the best TRF. The calibration errors  $\Delta T_{354.67}$  for each of SFP sets 1–5 are intercompared in Figs. 7, 8, 9, 10, 11, respectively.

A comparative analysis of  $\Delta T_{354.67}$  shows that in all five cases of SFP sets there are TRFs, the use of which is preferable for temperature retrievals and leads to smaller errors

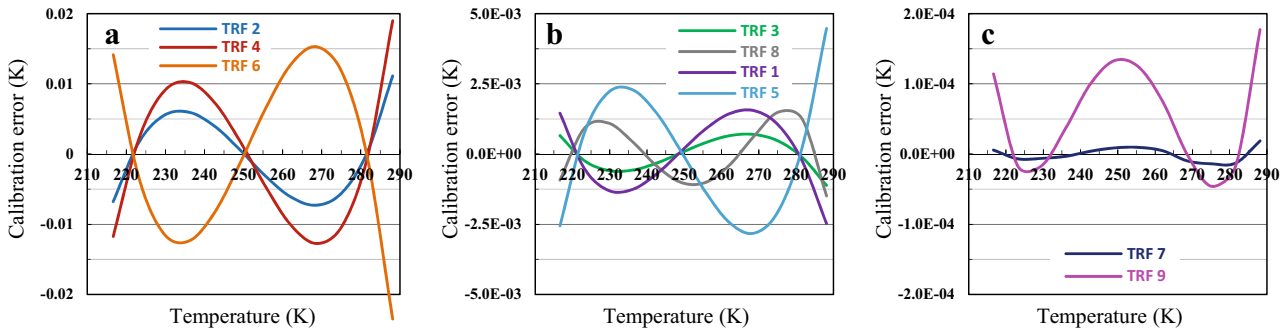


Fig. 10 Calibration errors  $\Delta T_{354.67}$  produced using TRFs 1–9 for SFP set 4 at  $\lambda = 354.67$  nm

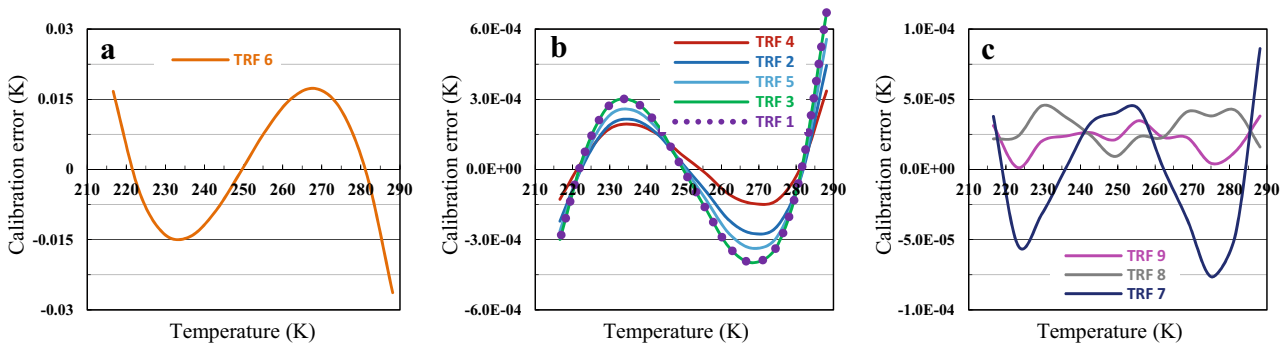


Fig. 11 Calibration errors  $\Delta T_{354.67}$  produced using TRFs 1–9 for SFP set 5 at  $\lambda = 354.67$  nm

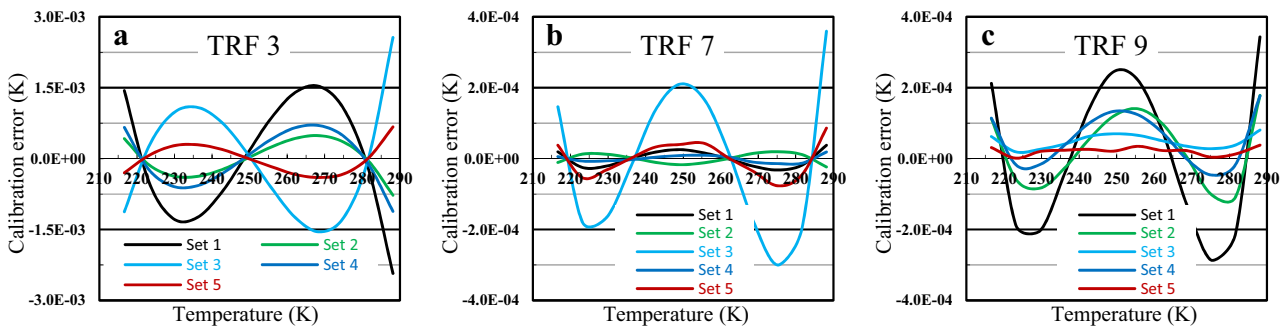
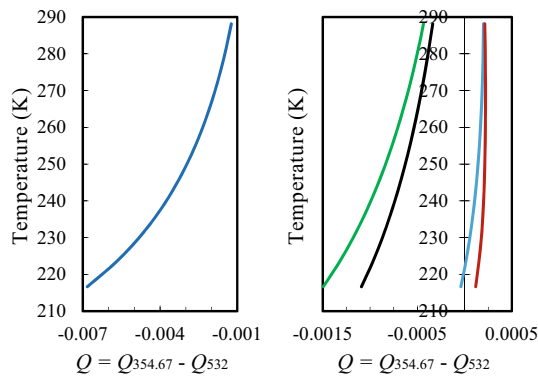


Fig. 12 Calibration errors  $\Delta T_{354.67}$  produced using TRFs 3, 7, and 9 for SFP sets 1–5 at  $\lambda = 354.67$  nm

than that of the other functions. TRF 3 gives the smallest errors of all three-coefficient TRFs 1–6 for SFP sets 1, 2, and 4 (Figs. 7b, 8b, and 10b), whereas TRF 1 and TRF 4 are the best three-coefficient functions for SFP sets 3 and 5 (Figs. 9b and 11b), respectively. Four-coefficient TRF 7 gives the smallest errors of all TRFs 1–9 for SFP sets 1, 2, and 4 (Figs. 7c, 8c, and 10c), whereas TRF 9 is the best function for SFP sets 3 and 5 (Figs. 9c and 11c). In total, as seen in Figs. 7, 8, 9, 10, 11, the use of TRFs 3, 7, and 9 for temperature retrievals consistently leads to small calibration

errors regardless of the SFP set. Namely,  $|\Delta T_{354.67}|$  does not exceed the value of  $3 \times 10^{-3}$  K when using TRF 3, while  $|\Delta T_{354.67}| < 4 \times 10^{-4}$  K for both TRFs 7 and 9 (Fig. 12). Note that the use of TRF 6 yields comparatively high calibration errors for all sets of SF passbands, especially for SFP set 5. This can be explained by the fact that the CF corresponding to TRF 6 does not satisfy the selection rules introduced in [17] for special cases of the GCF (7) and it was considered as an exception. Recall that this nonlinear CF cannot be reduced to the linear CF (2) when excluding



**Fig. 13** Tropospheric temperature vs the differences between the intensity ratios  $Q_{354.67}$  and  $Q_{532}$  calculated for each of SFP sets 1–5

from consideration all nonlinear effects caused by PRR lines broadening.

As follows from Fig. 12b, TRF 7 more accurately takes into account the contribution from broadened PRR lines to the signals detected in both lidar channels for four out of five SFP sets (excluding SFP set 3). Hence, TRF 7 can be considered as the function most suited for tropospheric temperature retrievals for any set of SF passband widths (for  $\lambda = 354.67$  nm). This is in agreement with the results obtained in [17] for temperature measurements using a PRR lidar at  $\lambda = 354.67$  nm.

### 6 Simulation results for $\lambda = 532$ nm

The simulation for  $\lambda = 532$  nm shows similar results as for  $\lambda = 354.67$  nm. Figure 13 presents the differences  $\Delta Q = Q_{354.67} - Q_{532}$  between the intensity ratios  $Q_{354.67}$  (Fig. 6) and  $Q_{532}$  (calculated at  $\lambda = 532$  nm) for each of SFP sets 1–5. For example, the value of  $Q_{354.67}$  varies between 3.5 and 7.5 for SFP set 5, while the corresponding  $|\Delta Q| < 2.5 \times 10^{-4}$ . Such small values of  $\Delta Q$  are explained by the following: as mentioned in Sects. 2.1 and 3.2, the molecular collision effect dominates over the Doppler one in the troposphere (Fig. 2) and the homogeneous collisional broadening of PRR lines does not depend on wavelength (see Eq. (30)). Therefore, the PRR line broadening provides almost the same contribution to channels  $J_{low}$  and  $J_{high}$  for the lidar wavelengths of 354.67 and 532 nm. This leads to close values of  $Q_{354.67}$  and  $Q_{532}$ .

For space considerations, the intercomparisons of calibration errors  $\Delta T_{532}$  produced using TRFs 1–9 for each of SFP sets 1–5 at  $\lambda = 532$  nm along with the differences  $\Delta T_{354.67} - \Delta T_{532}$  can be found in the electronic supplementary material. The errors  $\Delta T_{532}$  produced using TRFs 3, 7, and 9 and the differences  $\Delta T_{354.67} - \Delta T_{532}$  (Fig. 14) confirm the conclusion drawn for  $\Delta T_{354.67}$  (Fig. 12), i.e., TRF 7 is most suited for tropospheric temperature retrievals for any set of SF passband widths (for  $\lambda = 532$  nm). An intercomparison of  $\Delta T_{354.67}$  and  $\Delta T_{532}$  for TRFs 3, 7, and 9 (Figs. 12 and 14a–c) does not allow us to unambiguously determine the

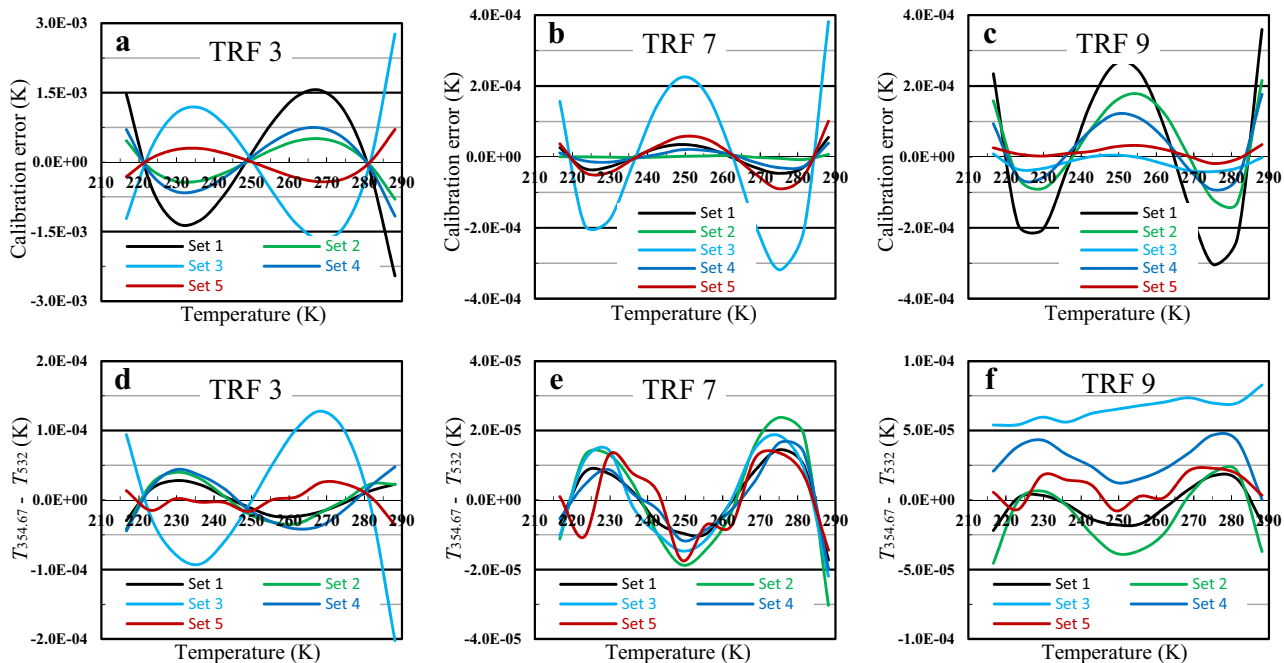


**Fig. 14** a–c Calibration errors  $\Delta T_{532}$  produced using TRFs 3, 7, and 9 for SFP sets 1–5 at  $\lambda = 532$  nm. d–f differences  $\Delta T_{354.67} - \Delta T_{532}$

best option from the considered sets of SF passband widths. However, the following can be stated: the use of SFP sets 1 and 3 results in larger calibration errors than that of SFP sets 2, 4, and 5.

## 7 Summary

In this study, we have calculated the ratios  $Q(T)$  of backscattered signal intensities from two PRR spectrum bands taking into account the collisional broadening of  $N_2$  and  $O_2$  PRR lines. The line broadening due to the Doppler effect was also considered using the HWHM  $\Delta \tilde{\nu}_{i,V}^{\text{FWHM}}/2$  of the pseudo-Voigt function instead of the Lorentzian HWHM  $\gamma_L/(2\pi c)$  in Eq. (36). The numerical simulation was performed for five frequently used sets of SF passband widths (Fig. 4, Table 1) and two laser wavelengths (354.67 and 532 nm). To obtain temperature profiles from the calculated ratios  $Q(T)$ , we applied nine nonlinear CFs (TRFs) in the temperature retrieval algorithm of the traditional PRR lidar technique.

The comparative analysis of the calibration errors  $\Delta T_{354.67}$  and  $\Delta T_{532}$ , produced using TRFs 1–9, and differences  $\Delta T_{354.67} - \Delta T_{532}$  for each of SFP sets 1–5 allow us to reveal the following:

- TRF 3 is the best function for tropospheric temperature retrievals of all three-coefficient TRFs 1–6 for SFP sets 1, 2, and 4, while TRF 1 and TRF 4 are the best ones for SFP sets 3 and 5, respectively;
- four-coefficient TRF 7 gives the smallest errors of all TRFs 1–9 for SFP sets 1, 2, and 4, whereas TRF 9 is the best function for SFP sets 3 and 5;
- when calculating the intensity ratios  $Q(T)$ , TRF 7 more accurately takes into account the contribution from broadened  $N_2$  and  $O_2$  PRR lines for four out of five SFP sets (excluding SFP set 3) at  $\lambda$  of 354.67 and 532 nm;
- the use of SFP sets 1 and 3 leads to larger calibration errors than that of SFP sets 2, 4, and 5;
- For two wavelengths (354.67 and 532 nm) and SFP sets 1–5, the absolute error  $|\Delta T|$  does not exceed the value of  $3 \times 10^{-3}$  K when using TRF 3, while  $|\Delta T| < 4 \times 10^{-4}$  K for both TRFs 7 and 9 (Figs. 12 and 14a–c).

In total, TRFs 3, 7, and 9 can be recommended for use in the temperature retrieval algorithm regardless of the lidar wavelength and set of SF passbands.

Despite two new techniques [18, 19] do not require lidar calibration with external temperature measurement instruments and have several advantages over the traditional technique, the accuracy of temperature retrievals can be increased by selecting TRFs 3, 9, or better TRF 7. Therefore, if one wants to measure tropospheric temperature with

an accuracy as high as possible, the traditional PRR lidar technique is the most preferable.

**Acknowledgements** The author thanks V.L. Pravdin for useful discussions of the work.

## Compliance with ethical standards

**Conflict of interest** The author declares that he has no conflict of interest.

## References

1. J. Cooney, J. Appl. Meteorol. **11**(1), 108 (1972)
2. Y.F. Arshinov, S.M. Bobrovnikov, V.E. Zuev, V.M. Mitev, Appl. Opt. **22**(19), 2984 (1983)
3. D. Nedeljkovic, A. Hauchecorne, M.L. Chanin, IEEE Trans. Geosci. Remote Sens. **31**(1), 90 (1993)
4. A. Behrendt, in *Temperature measurements with lidar*, ed. by C. Weitkamp. Lidar, range-resolved optical remote sensing of the atmosphere (Springer, New York, 2005), pp. 273–305
5. J. He, S. Chen, Y. Zhang, P. Guo, H. Chen, J. Geophys. Res. Atmos. **123**(19), 10925 (2018)
6. Q. Yan, Y. Wang, T. Gao, F. Gao, H. Di, Y. Song, D. Hua, Appl. Opt. **58**(19), 5170 (2019)
7. A. Behrendt, T. Nakamura, M. Onishi, R. Baumgart, T. Tsuda, Appl. Opt. **41**(36), 7657 (2002)
8. J. Su, M.P. McCormick, Y.H. Wu, R.B. Lee III, L.Q. Lei, Z.Y. Liu, K.R. Leavor, J. Q. Spectrosc. Radiat. Transf. **125**, 45 (2013)
9. H. Chen, S.Y. Chen, Y.C. Zhang, P. Guo, H. Chen, B.L. Chen, Opt. Express **23**(16), 21232 (2015)
10. R.K. Newsom, D.D. Turner, J.E.M. Goldsmith, J. Atmos. Ocean. Tech. **30**(8), 1616 (2013)
11. H. Chen, S.Y. Chen, Y.C. Zhang, P. Guo, H. Chen, B.L. Chen, J. Geophys. Res. Atmos. **121**(6), 2805 (2016)
12. J. He, S. Chen, Y. Zhang, P. Guo, H. Chen, Opt. Commun. **452**, 88 (2019)
13. A. Behrendt, J. Reichardt, Appl. Opt. **39**(9), 1372 (2000)
14. R.B. Lee III, Tropospheric temperature measurements using a rotational Raman lidar (PhD dissertation) (Ann Arbor, ProQuest LLC, 2013) 112 pp. <https://pqdtopen.proquest.com/doc/1437652821.html?FMT=ABS>. Accessed 21 Sep 2020
15. V.V. Gerasimov, V.V. Zuev, Opt. Express **24**(5), 5136 (2016)
16. V.V. Zuev, V.V. Gerasimov, V.L. Pravdin, A.V. Pavlinskiy, D.P. Nakhitgalova, Atmos. Meas. Tech. **10**(1), 315 (2017)
17. V.V. Gerasimov, Appl. Phys. B **124**(7), 134 (2018)
18. M. Weng, F. Yi, F. Liu, Y. Zhang, X. Pan, Opt. Express **26**(21), 27555 (2018)
19. S. Mahagammulla Gamage, R.J. Sica, G. Martucci, A. Haefele, Atmos. Meas. Tech. **12**(11), 5801 (2019)
20. E. Hammann, A. Behrendt, Opt. Express **23**(24), 30767 (2015)
21. U. Wandinger, in *Raman Lidar*, ed. by C. Weitkamp. Lidar, range-resolved optical remote sensing of the atmosphere (Springer, New York, 2005), pp. 241–271
22. R.M. Measures, *Laser remote sensing, fundamentals and applications* (Wiley, New York, 1984)
23. M. Radlach, A. Behrendt, V. Wulfmeyer, Atmos. Chem. Phys. **8**(2), 159 (2008)
24. Y.I. Gerasimov, *Course in Physical Chemistry*, Vol. 2 (Khimiya, Moscow, 1973), p. 624 (in Russian)
25. J.J. Olivero, R.L. Longbothum, J. Quant. Spectr. Rad. Transfer **17**(2), 233 (1977)

26. C.M. Penney, R.L. St. Peters, M. Lapp, *J. Opt. Soc. Am.* **64**(5), 712 (1974)
27. Y.J. Li, S.L. Song, F.Q. Li, X.W. Cheng, Z.W. Chen, L.M. Liu, Y. Yang, S.S. Gong, *Chinese. J. Geophys.* **58**(4), 313 (2015)
28. D. Wu, Z. Wang, P. Wechsler, N. Mahon, M. Deng, B. Glover, M. Burkhart, W. Kuestner, B. Heesen, *Opt. Express* **24**(18), A1210 (2016)
29. Y.J. Li, X. Lin, S.L. Song, Y. Yang, X.W. Cheng, Z.W. Chen, L.M. Liu, Y. Xia, J. Xiong, S.S. Gong, F.Q. Li, *IEEE Trans. Geosci. Remote Sens.* **54**(12), 7055 (2016)
30. Y.J. Li, X. Lin, Y. Yang, Y. Xia, J. Xiong, S.L. Song, L.M. Liu, Z.W. Chen, X.W. Cheng, F.Q. Li, *J. Quant. Spectrosc. Radiat. Transf.* **188**(2), 94 (2017)
31. P. Achtert, M. Khaplanov, F. Khosrawi, J. Gumbel, *Atmos. Meas. Tech.* **6**(1), 91 (2013)
32. A. Behrendt, T. Nakamura, T. Tsuda, *Appl. Opt.* **43**(14), 2930 (2004)
33. J.Y. Jia, F. Yi, *Appl. Opt.* **53**(24), 5330 (2014)
34. P.A. Bazhulin, *Sov. Phys. Usp.* **5**(4), 661 (1963)
35. <https://ntrs.nasa.gov/archive/nasa/casi.ntrs.nasa.gov/19770009539.pdf>. Accessed 21 Sep 2020

**Publisher's Note** Springer Nature remains neutral with regard to jurisdictional claims in published maps and institutional affiliations.